Size-dependent photon avalanching in Tm^{3+} doped $LiYF_4$ nano, micro and bulk crystals

Magdalena Dudek[$], Marcin Szalkowski[$], Małgorzata Misiak, Maciej Ćwierzona, Artiom Skripka, Zuzanna Korczak, Dawid Piątkowski, Piotr Woźniak, Radosław Lisiecki, Philippe Goldner, Sebastian Maćkowski, Emory M. Chan, P. James Schuck, Artur Bednarkiewicz[*]

$ these authors contributed equally

M. Dudek

Institute of Low Temperature and Structure Research, Polish Academy of Sciences, Okólna 2, 50-422 Wroclaw, Poland

M. Szalkowski

Institute of Low Temperature and Structure Research, Polish Academy of Sciences, Okólna 2, 50-422 Wroclaw, Poland

M. Misiak

Institute of Low Temperature and Structure Research, Polish Academy of Sciences, Okólna 2, 50-422 Wroclaw, Poland

M. Ćwierzona

Institute of Physics, Faculty of Physics, Astronomy and Informatics, Nicolaus Copernicus University, Grudziądzka 5, 87-100 Toruń, Poland

A. Skripka

The Molecular Foundry, Lawrence Berkeley National Laboratory, Berkeley, CA, USA

Nanomaterials for Bioimaging Group, Departamento de Física de Materiales, Facultad de Ciencias, Universidad Autónoma de Madrid, Madrid, 28049, Spain

Z. Korczak

Institute of Low Temperature and Structure Research, Polish Academy of Sciences, Okólna 2, 50-422 Wroclaw, Poland

D. Piątkowski

Institute of Physics, Faculty of Physics, Astronomy and Informatics, Nicolaus Copernicus University, Grudziądzka 5, 87-100 Toruń, Poland

P. Woźniak
Institute of Low Temperature and Structure Research, Polish Academy of Sciences, Okólna 2, 50-422 Wroclaw, Poland

R. Lisiecki
Institute of Low Temperature and Structure Research, Polish Academy of Sciences, Okólna 2, 50-422 Wroclaw, Poland

P. Goldner
Chimie ParisTech, PSL University, CNRS, Institut de Recherche de Chimie Paris, 75005 Paris, France

S. Maćkowski
Institute of Physics, Faculty of Physics, Astronomy and Informatics, Nicolaus Copernicus University, Grudziądzka 5, 87-100 Toruń, Poland

E. M. Chan
The Molecular Foundry, Lawrence Berkeley National Laboratory, Berkeley, CA, USA

P. J. Schuck
Department of Mechanical Engineering, Columbia University, New York, NY, USA

A. Bednarkiewicz
Institute of Low Temperature and Structure Research, Polish Academy of Sciences, Okólna 2, 50-422 Wroclaw, Poland, E-mail: A.Bednarkiewicz@intibs.pl

Keywords: photon avalanche, lanthanides, up-conversion, super-resolution imaging, nanocrystals, microcrystals

Abstract

Photon avalanche (PA) is a highly nonlinear mode of up-conversion that is characterized by 100-1000-fold increase in luminescence intensity upon minute increments of pumping power. In light of numerous possible nano-bio-technology applications and demand for information about the susceptibility of the PA phenomenon to the material volume and surface effects, here the PA emission is investigated and theoretically modeled. The two-color, highly non-linear PA emission at 475 and 800 nm is clearly observed in bulk single crystal, individual microcrystals, and ensembles of colloidal core and core-shell nanoparticles of $LiYF_4$ host doped with either 3 or 8% of thulium ions. The properties of PA emission, such as PA non-linearity (S=6-12), PA gain (ca.100-300), PA intensity and luminescence kinetics in these materials show dependence on crystal volume and surface quenching. Theoretical simulations support understanding of key physical processes that influence PA performance. Moreover, photon avalanche single beam super-resolution imaging (PASSI) is realized for the first time in 3% Tm^{3+} doped $LiYF_4$ core-shell nanoparticles. The obtained insights and predictions form a solid background for further development and applications of new optimized PA materials.

1. Introduction

Lanthanide doped materials are capable of efficiently converting low energy near infrared (NIR) excitation to shorter wavelength radiation in the ultraviolet, visible, and NIR spectral ranges.[1] This anti-Stokes process of up-conversion (UC) is much more efficient than harmonic generation or multiphoton absorption, owing to the sequential absorption of photons by real and long-lived excited states.[2] Such materials exhibit interesting nonlinear optical responses because luminescence intensity I_{LUM} scales with the excitation power I_P as $I_{LUM} \sim (I_P)^S$, where the nonlinearity factor S is typically between 2 and 5. Various mechanisms may be responsible for UC emission, including excited state absorption (ESA), energy transfer up-conversion (ETU), cooperative absorption (CA) or luminescence (CL), cooperative sensitization (CET), as well as photon avalanche (PA) – which is the focus of this work.[2] While the majority of these up-conversion mechanisms `U, ESA, CA, CL, CET) has been widely studied and they are well understood across a range of bulk and nanosized materials, the PA emission has been almost exclusively studied in bulk single crystals or fibers, and mostly only at cryogenic temperatures.

There are two requirements for lanthanide doped luminescent materials to unveil PA emission. The first one is a high rate between excited state (σ_{ESA}) and ground state absorption (σ_{GSA}) cross-sections. It is often assumed that $\beta = \sigma_{ESA}/\sigma_{GSA}$ (**Equation 1**) should be higher than

10 000.[3] Secondly, an efficient energy looping processes must enhance the population of an intermediate level (from which ESA originates) through cross relaxation (CR) between neighboring ions. CR is typically augmented by increasing the concentration of the dopants. The combination of high β and efficient CR yields two important characteristics that distinguish PA from other UC modes. First, PA systems exhibit an exceptionally steep dependence of the emission intensity on pump power. Several orders of magnitude increase in emission intensity is induced by a fractional increase of the pump power above the PA threshold. Second, near its threshold, PA is characterized by slow emission risetimes, τ_R, being the result of the multistep looping of energy within dopants (via CR) before emission . The value of τ_R reaches even hundreds of milliseconds at PA thresholds and gets shorter as the power is further increased. Importantly, both these highly nonlinear characteristics of the PA emission should be more susceptible to any perturbation occurring during the energy looping as compared to other lanthanide-doped luminescent or upconverting materials. [4–6]

The PA effect was first observed in $LaCl_3$ single crystals doped with praseodymium ions.[7] Shortly after, PA emission was demonstrated in bulk materials doped with various lanthanides (almost always at cryogenic temperatures[3]) in the context of UC lasing[3,8] or quantum counters.[7] However, current research of UC materials concerns frequently biomedical applications, which require nanometer-size colloids that can be suspended in solution and conjugated to analytes. Synthetic methods to obtain lanthanide-doped upconverting nanoparticles (UCNPs) have been developed, and the rational control of spectral properties have been mastered through core-shell designs[9–14] and through better understanding of energy migration and dopant distributions in nanocrystals[15–20]. Unfortunately, since the discovery of PA in 1979 no clear evidence of PA emission at the nanoscale has been observed in conventional Yb^{3+} sensitized UCNPs co-doped with - Tm^{3+}/Er^{3+}/Ho^{3+} activators. Only recently PA has been demonstrated in colloidal avalanching nanoparticles (ANPs) at room temperature.[21] PA at 800 nm emission was achieved under 1064 nm or 1450 nm photoexcitation by employing $NaYF_4$ nanoparticles with cores heavily doped with Tm^{3+} ($\geq$ 8%; typically, up to few-tens-fold more than in conventional Yb^{3+} sensitized Tm^{3+} upconverting nanomaterials). Achieving PA at the nanoscale opens a wide range of applications, such as sub-diffraction imaging[21–23], biosensing, nanothermometry[22,24], anti-counterfeiting[25], and (up-converting) nano- and micro- lasers[26]. Therefore, in order to control the PA effect and tailor it to the particular requirements, fundamental studies must be conducted to elucidate the chemical and physical factors that affect PA emission.

In this work, we, for the first time, observe two color, highly nonlinear PA emission of Tm^{3+} at 475 and 800 nm. Moreover, the influence of crystal size on the PA of Tm^{3+}-doped $LiYF_4$ photon avalanching materials is studied, with a focus on key properties such as the PA threshold, nonlinearity slope, emission gain and luminescence dynamics. For that purpose, we synthesized and quantitatively compared the PA of 3% Tm^{3+}-doped materials at three different length scales: microcrystals and nanocrystals (both not passivated cores and surface-passivated core-shell nanocrystals) were compared with the 3% Tm^{3+}-doped bulk crystal. Additionally, corresponding $LiYF_4$ micro and nanomaterials doped with higher Tm^{3+} content, i.e., 8% Tm^{3+}, were synthesized and quantitatively compared to 8% Tm^{3+}-doped $NaYF_4$ core-shell ANPs.[21] Moreover, versatile and critical analyses of the PA phenomenon in such a wide range of sizes aiming to understand the role of the sample volume under PA excitation conditions was carried out. Additionally, the differential rate equation (DRE) model was used to understand *in silico* how the phenomenological parameters of the materials may affect the PA emission. ~~Without tedious synthesis~~ we were able to predict some trends and directions to follow to play with the non-linearity and pump power response. Finally, in super-resolution imaging of individual ANPs, we show that one does not need extreme non-linearities (>15) to image nanoobject well below limit of diffraction. These studies shine new light on the role of size and surface area on PA.

2. Results and discussion

2.1. Understanding the role of pump power and doping concentration

To investigate influence of host size and architecture influence on PA, a size series of $LiYF_4$ bulk crystal, microcrystals, core nanocrystals, and core-shell nanocrystals was synthesized with Tm^{3+} doping levels of 3% or 8%. In this way we are able to compare bulk, micro and nanocrystals (both core and core-shell) at the same composition of 3%. The experiments aimed at comparing the PA effect in $LiYF_4$ microcrystals, core and core-shell nanocrystals doped with 8% Tm^{3+} were motivated by choosing the concentration which has been found optimal for PA phenomenon in a similar $NaYF_4$ matrix.[21] The choice of materials is further justified, as concentrations below 3% reduces the energy looping and may hinder PA, while concentrations above 8% did not show substantial improvement in PA performance due to enhanced concentration quenching.

Crystal purity, size and morphology of all the samples were confirmed by XRD and electron microscopy (**Figures S1, S2, S3**, and **Figure 1)**.

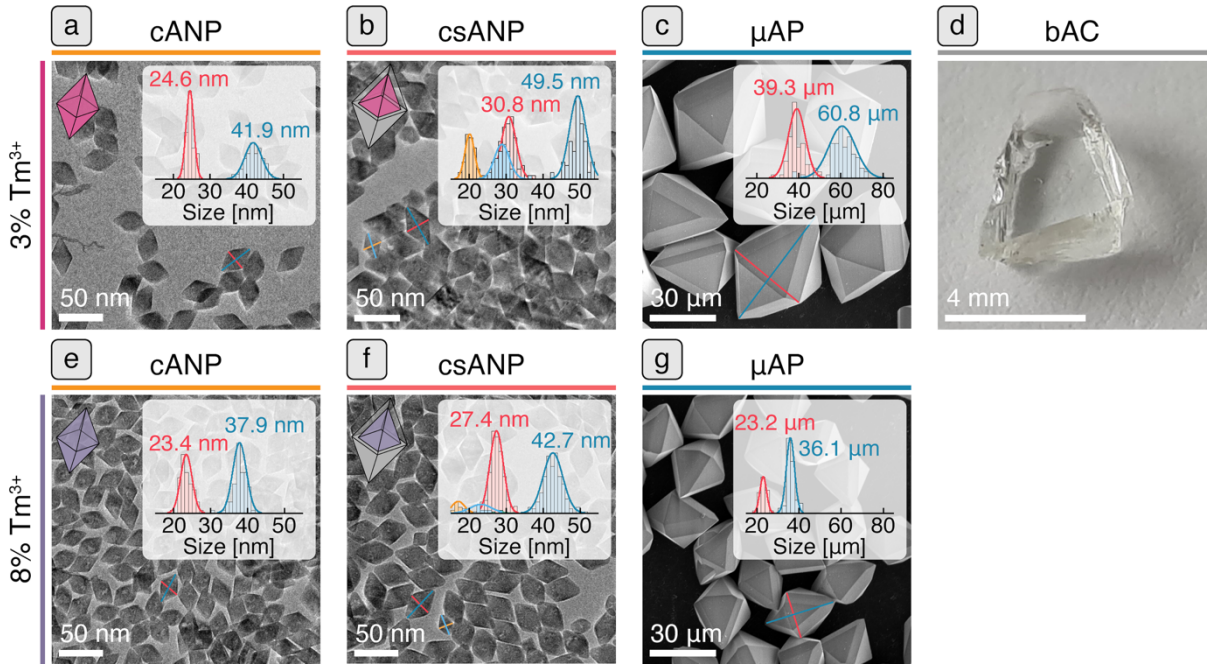

Figure 1. Comparison of morphology of cANP (a, e), csANP (b, f), mAP (c, g) and bAC (d) $LiYF_4$ crystals doped with 3% or 8% of Tm^{3+}. Based on average dimensions of the nanocrystals, the thickness of the shell is 3.1 and 2 nm in width and 3.8 and 2.4 nm in length, for 3% Tm^{3+} and 8% Tm^{3+} doped csANPs, respectively.

Table 1. Morphological parameters for Tm^{3+}-doped core avalanching NPs (cANP = Tm^{3+}:$NaYF_4$), core-passive shell avalanching NPs (csANP = Tm^{3+}:$NaYF_4$@$NaYF_4$), Tm^{3+}-doped avalanching microparticles (µAP) and bulk avalanching crystal (bAC).

		3% Tm^{3+}		8% Tm^{3+}		
	Diagonal	Size	Shell thickness	Size	Shell thickness	units
cANP	short	24.6 ± 1.1		23.4 ± 1.6		[nm]
	long	41.9 ± 2.3		37.9 ± 1.8		[nm]
csANP	short	30.8 ± 2.0	3.1	27.4 ± 1.8	2.0	[nm]
	long	49.5 ± 2.2	3.8	42.7 ± 2.7	2.4	[nm]
µAP	short	39.3 ± 4.0		23.2 ± 1.6		[µm]
	long	60.8 ± 6.3		36.1 ± 1.9		[µm]
bAC		~3				[mm]

Next, the optical properties of all these materials were studied with identical optical setup and methodology. Experiments were performed on nanoparticles drop-cast as thick films on a glass slide and the signal was averaged from 10 measurements on different spots on the slide. The experiments on µAP were performed on individual microparticles, while the sample position against the excitation beam was optimized for the highest signal intensity. Based on

the experimentally determined power dependent PA properties for 3% and 8% Tm^{3+} doped materials (**Figure 2** for 800 nm PA emission and **Figure S4** for 475 nm PA emission), respective figures of merit were derived in **Figure S5**. The experimental approach applied here is more comprehensive and versatile than the characterization proposed previously – namely we separately analyze the plots of the pump power dependent non-linearity slopes $S(I_P)$, PA gains $D_{AV}(I_P)$, and luminescence risetime kinetics $t_{50\%}(I_P)$, which used to be presented in a very simplified way as just single numbers. This new approach provides better understanding of the power dependence curves and also makes the analysis more objective. The highest values of the nonlinearity (S_{MAX}), highest values of PA gain ($D_{AV\,MAX}$), and longest luminescence risetimes ($\tau_{R\,MAX}$) were calculated (**Figure S5a, b, c**). Moreover, the pump power intensities, at which those S_{MAX}, $D_{AV\,MAX}$ and $\tau_{R\,MAX}$ parameters were found, are presented in **Figure S5d, e and f**, respectively. Importantly, we found that Tm^{3+} are capable to generate PA emission not only at 800 nm from $^3H_4$ level (**Figure 2**), as shown previously, but also at 475 nm from $^1G_4$ level (**Figure S4, Table S1**). Both emissions exhibited highly nonlinear dependence of intensity and risetime on the pump power– the characteristic features of the PA. Such an avalanche behavior of the blue emission (475 nm) is caused by the fact that the $^1G_4$ level population builds up by combing ~~draft horse role of~~ energy looping and photon avalanche between $^3H_{6,5,4}$ levels (**Figure 4a**, black arrows) with ESA mechanism (**Figure 4a**, light grey arrows) ($^3H_4 + h\nu \rightarrow {}^1G_4$). The PA emission at 475 nm was ca. 100-fold dimmer than the 800 nm emission (**Figure S4**). The observation of 475 nm PA avalanche emission gives promise to design more PA colors using other lanthanide co-dopants, but careful optimization of the co-dopant concentrations and distribution must be performed in order to find balance between the looping and ET to other ions, aiming to minimize parasitic destruction of the looping mechanism by additional energy acceptors[4].

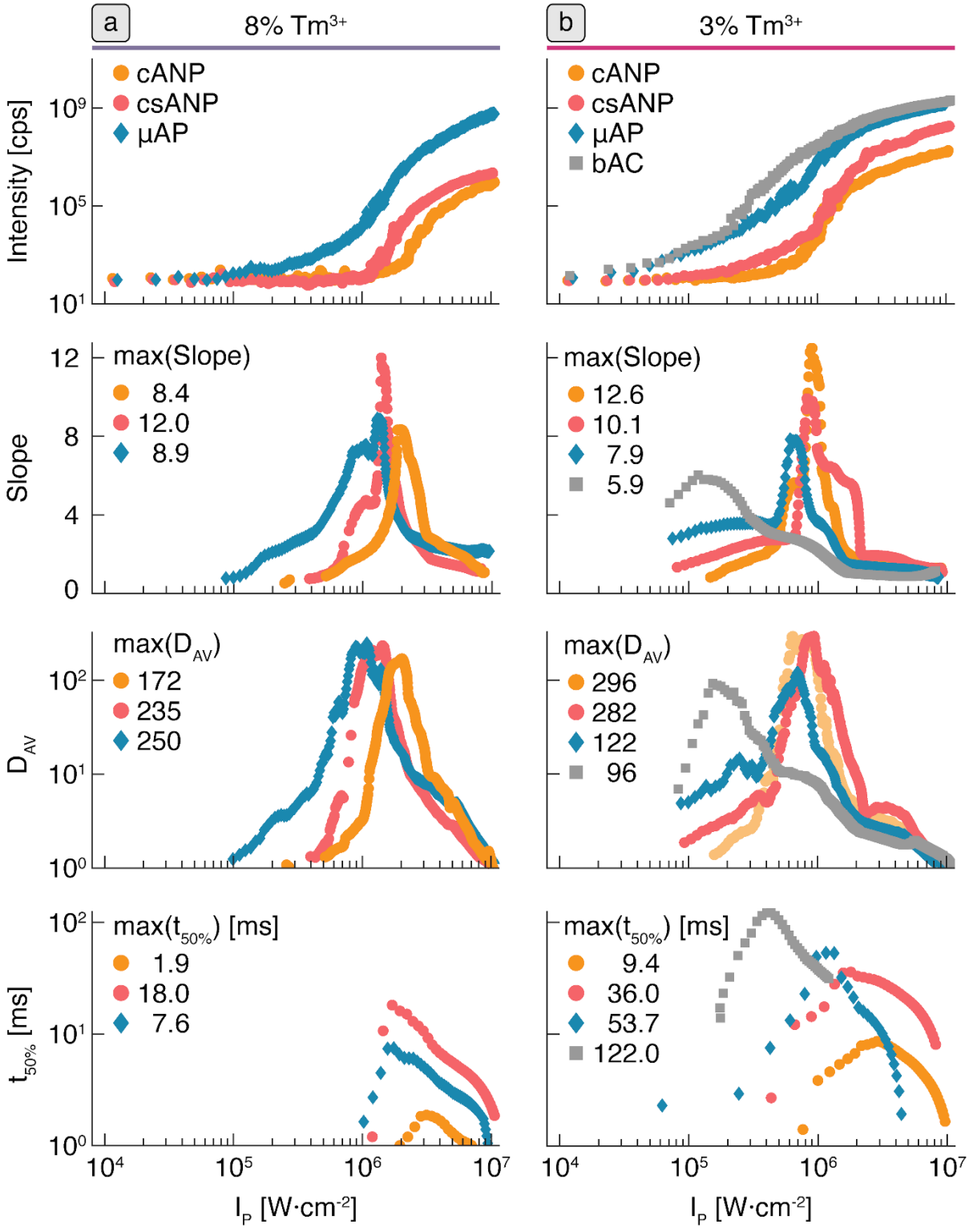

Figure 2. Thulium photon avalanche behavior in nano, micro and bulk crystals. Comparison of pump power dependent PA emission intensity (row 1), PA slopes (row 2), PA gains (row 3) and 50% risetimes (row 4) at 800 nm for the 8% (a) and 3% (b) Tm^{3+} doped materials cANP, csANP, µAP, and bAC. Corresponding graphs showing the 475 nm PA emission are presented in **Figure S4**.

Similar to conventional up-conversion,[27] PA emission is the result of complex, collective dynamics and that of balance between the rates of CR (required for PA), EM (energy migration leading to energy loses), radiative emission, and non-radiative losses (either through multiphonon relaxation or surface quenching). It is important to note that there are two highly relevant factors regulating the energy distribution throughout the host material. First, while the distance between the interacting ions (directly related to the ions concentration) strongly influences their CR rate, the geometrical borders of the host also naturally limit the energy migration.[28] **Figure 3** schematically presents the mechanisms which are essential for understanding the photo physics of the PA materials and for the PA performance (such as ESA, CR, EM, quenching (Q) and PA emission, **Figure 3a**), and the role of various doping concentrations for both low (**Figure 3b**) and high (**Figure 3c**) pumping power regimes (below and above the pump power threshold value, respectively).

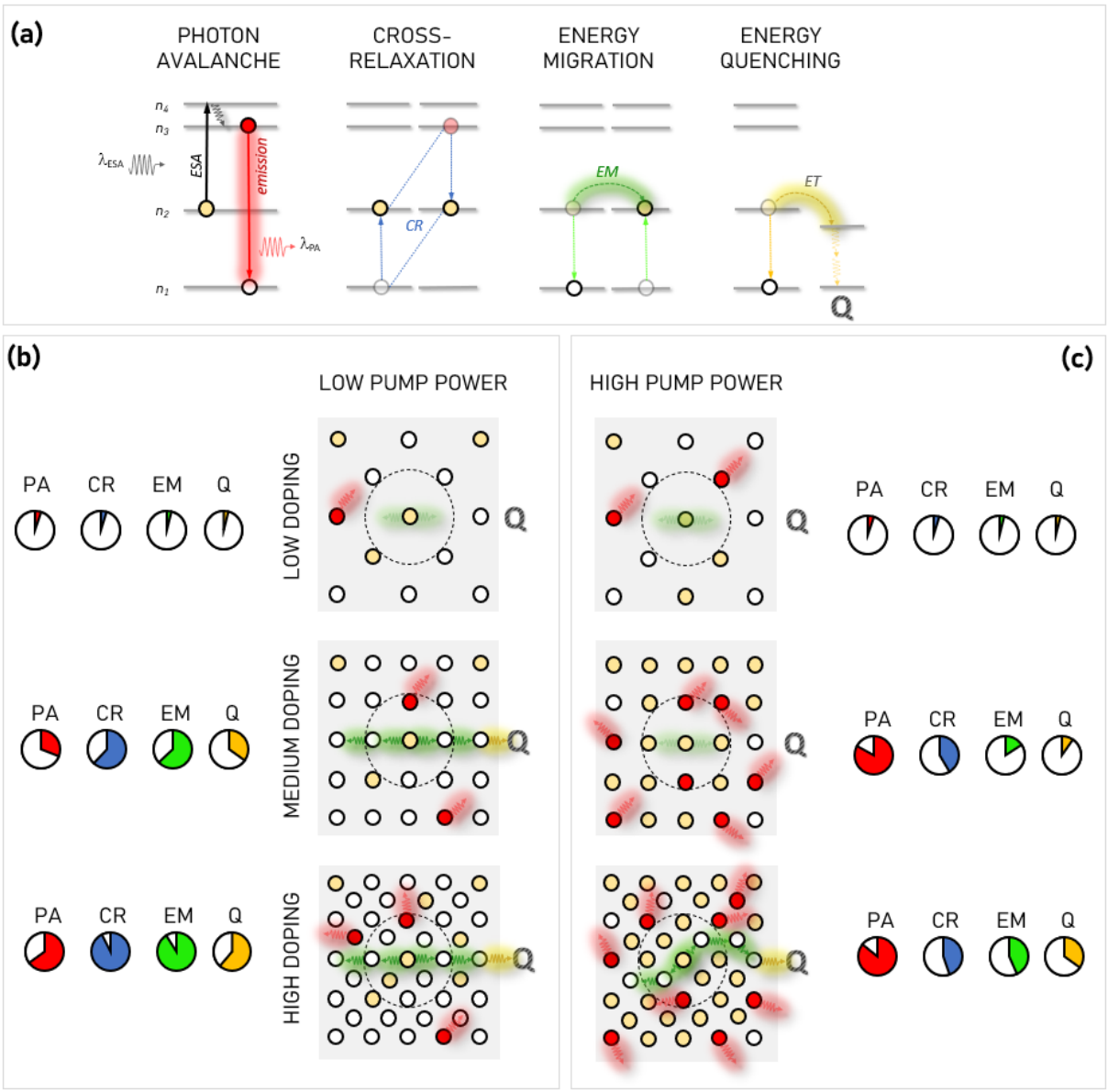

Figure 3. Comparison of the most important effects observed in the experiments (a) and scheme of the relative populations of ions in various energetic states and resulting probabilities of the mechanisms to occur in low (b) and high (b pumping power regimes. Three various concentrations of optically active Tm^{3+} dopants were considered from both regimes. The range of efficient interaction of one of the ions with neighboring ions was marked with black dashed circle. The semi-quantitative indicators of the probability of the considered phenomena (PA, CR, EM, Q) are presented for these various configurations.

For low dopant concentrations, the large average separation between neighboring ions prevents efficient CR and EM interactions, thus no PA emission should be observed except linear side-band ESA absorption and linear emission. One can expect that increasing the

concentration of Tm^{3+} ('medium doping' in **Figure 3**) will enhance CR, resulting in increased population of the ions in the intermediate energetic state (state n_2 in **Figure 3**). In such circumstances, higher pumping power should satisfy all prerequisites for PA to occur, such as gradually rising ESA efficiency and composition defined energy looping. The augmented population of the ions in the n_2 state enables the absorption of further excitation quanta and promotion of electrons from the n_2 to n_3 state. At high pump powers, population inversion ($n_2 + n_3 > n_1$) may occur, thus the CR process becomes inefficient, making PA emission or quenching the most probable scenario.

Interesting relationships might be expected when analyzing both pumping regimes in the context of energy migration (EM). For pump powers below the PA threshold, EM competes with CR and might result in energy migration toward quenchers present at the surface of the host. However, increased pumping power successfully hinders EM at longer distances, as most of the nearby ions are in the same energy state and thus are not able to exchange the energy with neighboring ions. As a result, the energy pumped into the system becomes highly localized and reduces the probability of energy diffusion toward external quenchers. Therefore, due to reduced energy losses in the energy looping regime, the passive shell does not critically impact the PA performance; in particular shells do not significantly modify the observed threshold or nonlinearity of optical responses. Nonetheless, the quenching of excited ions located at the surface should still be expected. Interestingly, increasing the concentration of dopants even further ('high concentration' in **Figure 3**) should change the situation significantly. As the density of the optically active ions increases, the number of the interacting ions and therefore the probability of interactions to occur is also enhanced. It is more difficult to saturate such a system and even at high pumping regime the probability of finding an EM path to surface quenchers is still high. This implies long-distance EM combined with lack of the protective shell may lead to reduced PA efficiency and a shift in the corresponding power dependence toward higher pumping power densities (and higher pump thresholds required to initiate PA emission).

This hypothesis is somehow counterintuitive when the avalanche effect is compared with the issues known in UCNPs. However, in UCNPs, energy migration is efficient due to the large (ca. 9400 cm^{-1}) energy gap between the two Yb^{3+} energy manifolds, and this EM may be interrupted when activator ions or crystallographic defects lay on the EM path or when diffused energy reaches the surface of NP [28]. But the situation in PA regime is different. This is because

under intense 1064 nm pumping above the PA threshold, the ESA ($^3H_4 + h\nu \rightarrow {}^3F_2$) and CR ($(^3H_4; {}^3H_6) \rightarrow ({}^3F_4; {}^3F_4)$) processes compete with each other and with EM. Oppositely, under low intensity excitation, the crystals are transparent at 1064 nm excitation wavelength. When this latter fact is combined with the low population of $^3H_6$ level, the CR mentioned above becomes ineffective and only ESA may play a role.

The manifestation of these effects can be found in the results presented here, both in terms of PA thresholds and corresponding maximal $t_{50\%}$ values, as well as for observed luminescence intensities (**Figure 2**). A clear size dependent trend of the luminescence intensity, the slopes and PA thresholds can be found in the 8% Tm^{3+}-doped cANP, csANP and μAP samples. However, the $\tau_{50\%}$ is the shortest for the cANP which may indicate that the losses are overwhelming the energy looping and PA emission, allowing it to reach steady state faster. For smaller structures, the accessible volume for the energy spreading is lower. Therefore the scenario, in which ions in emitting states have no ground state neighbors for energy exchange (making emission the only probable way of energy dissipation) is established much faster. Considering the 3% Tm^{3+} doped samples, the size dependent relationships are also clearly observed, but the interpretation of qualitative (**Figure 2**) and quantitative (**Figure S5**) results is less intuitive than for the 8% Tm^{3+} samples. As soon as the volume of PA material (V_{PA}) decreases from bulk through microcrystals to nanocrystals, the PA threshold increases progressively by nearly 1 order of magnitude, from c.a. 200 kW cm^{-2} (for bulk), to 300-400 kW cm^{-2} (for μAP), and 700-800 kW cm^{-2} (for cANP and csANP).

Moreover, significant differences related to the role of passive shell around the Tm^{3+}-doped ANP core nanoparticles were found for the two analyzed architectures of the nanocrystals. The deposition of a passivating shell on the 3% Tm^{3+} doped nanoparticles changes neither the threshold pump power, nor does it significantly improve PA performance (in terms of S values and D_{AV}); however it does improve the brightness ca. 10-fold. Moreover, ca. 8-fold longer risetimes are observed in csANP compared to bare cANP. Such a behavior suggests these effects should owe to the concentration of Tm^{3+}, because in 8% Tm^{3+} doped sample the passive shell around cANP produces different set of effects, namely lowers the PA threshold and enhances the nonlinearity. These latter effects in 8% ANPs are consistent with expectations and can be understood in terms of protective role of the shell in reducing surface quenching.[5] Our samples were passivated with ca. 3-4 nm thick shell (for the 3% sample) and ca. 2-2.5 nm thick shell for the 8% samples. It is known, that variations of the shell thickness from 3 to 9 nm

resulted in significant variations of the PA behavior in individually studied 8% Tm^{3+} $NaYF_4$ csANP[5]. For 3% Tm^{3+} samples, one may note an inverse correlation between the risetimes length and maximum nonlinearities (*S*). In 8% Tm^{3+} samples, where the CR processes become stronger at the cost of both EM and emission, this relationship deviates from the trend found in less concentrated samples.[28] In both cases the shortest risetimes are found for cANP. Interestingly, higher nonlinearities and larger PA thresholds are found for smaller materials, which can potentially be ascribed to augmented surface/ligand phonon assisted quenching and GSA as well as to disturbance to crystal field (and thus to A_2) found for superficial lanthanides.[29] Moreover, one cannot exclude ion intermixing between doped core and passive shell and inhomogeneity of lanthanides distribution[30], which might further complicate the analysis.

Simultaneously, the thulium luminescence decays (**Figure S6**) progressively get shorter in the order bAC > µAP > csANP > cANP within both 3 and 8 % Tm^{3+} doping series, as well as the luminescence decay kinetics of the 8% samples are shorter than in the corresponding 3% crystals. This confirms that surface quenching is an issue, and is indeed reduced by the surface passivation with the shell. Because the 'S' power dependence and the derived S_{MAX} value of ~10-12 and D_{AV} values ~200 are comparable for cANP and csANP, we speculate that the PA phenomenon is highly volume-confined in 3% Tm^{3+} doped samples. Interestingly, the nonlinearity (S-factor) as well as PA gain (D_{AV}) are higher for 3% Tm^{3+}-doped nanoparticles (ca. 10 for both core and core-shell) as compared to equally doped micro (S~8, D_{AV}~100) and bulk (S~6, D_{AV}~100) crystals (**Figure 2**). In the 8% doped cANP, csANP and µAP, the PA gains are similar to the 3% samples and go up to 200. At the same time, the pump power threshold, at which the PA nonlinearity emerges, is the lowest for the bulk materials. Such effects may be partially caused by the geometric relation between the material of a given size and the focused spot of the laser beam, as illustrated schematically in **Figure S7**. Furthermore, the S values determined for 3% Tm^{3+} doped samples are relatively high considering that Lee *et al.* reported slopes of only 5.1 and 6.7 for the 1% and 4% Tm^{3+} doped $NaYF_4$, respectively.[21] On the other hand, the nanoparticles studied here are slightly larger, so it might not be a valid comparison to understand whether low Tm^{3+} doping in $LiYF_4$ affords similar PA as higher doping in $NaYF_4$, or if this is related to crystal symmetry differences of the two hosts. Average inter-ion distance in both structures is quite similar, of around 4.1 Å, so we should look for other explanations, such as the spectral match of excitation beam to ESA (here 1059 nm, see calculated ESA spectra **Figure S8**), the $\sigma_{ESA}/\sigma_{GSA}$ in both matrices at given wavelengths, or the

random polarization of excitation beam used here for the $LiYF_4$. Lower nonlinearities, ca. 5-fold larger PA thresholds, and 6-300-fold shorter risetimes for the same 8% Tm^{3+} doped samples in $LiYF_4$, as compared to previous studies in colloidal nano Tm^{3+} $NaYF_4$, X=8..100% (6-12 vs 5-31.6, respectively)[21], may originate from different crystal field splitting of Tm^{3+} in these $LiYF_4$ or $NaYF_4$ hosts, and the resulting differences in excitation wavelength spectral matching to ESA between the two host materials.

Very similar properties and relationships were found for Tm^{3+} emission at 475 nm (reference to Fig). This observation is quite understandable because this ($^3H_4$; $^3H_6$) → ($^3F_4$; $^3F_4$) CR process feeds the $^3F_4$ excited state of Tm^{3+}, which is actually the workhorse mechanism behind the PA emission and nonlinear features. All further Tm^{3+} emission bands, such as the ones originating from the $^3H_4$ level (800 nm) or $^1G_4$ level ($^3H_4$+1064 nm→$^1G_4$→475 nm) under PA photoexcitation scheme at 1059 nm, stem from population of the same 'nonlinear' $^3H_4$ level and thus results in similar PA slopes at 800 nm (**Figure 2**) and at the 475 nm (**Figure S4**). This effect not only increases the number of possible PA colors emitted by Tm^{3+} ions, but may also allow a purposeful manipulation of the accumulated energy and population of other lanthanides to increase number of highly nonlinear PA colors produced by a single excitation wavelength. The latter would be a valuable capability for super-resolution multiplexed imaging.

Equally interesting relationships can be found in the emission risetimes (see **Figure S9** and **Figure S10**, **Table S2**). Characteristic slowing down at the PA threshold, followed by a decrease of luminescence risetimes for saturation region was observed. The risetimes reflect the looping nature of energy accumulation in the excited states of Tm^{3+}. Qualitatively the risetimes reflect a complex balance resulting from the size (volume and lack of boundaries for energy migration), quenching (surface protection/defects/quenching sites) and concentration of Tm^{3+} (i.e. CR rate and number of CR interactions, balance between CR and EM) that ultimately define the time of looping. Slower risetimes should be correlated with efficiency of CR (check 3 vs 8%) as well as with the size (increased energy-migration in bulk, and micro particles delays the population build-up for PA). In general, the maximum $t_{50\%}$ risetimes are getting shorter in the order of bAC (~100 ms) > µAP (~ 50 ms) > csANP (~40 ms) > cANP (~9 ms). The intuition suggests that increased losses (whose contribution follows the opposite trend, i.e., along the bAC < µAP < csANP < cANP series) increase perturbation of photon looping and should, in principle, gradually hinder PA process. When going from bACs to cANPs, the influence of size

is significant: luminescence intensity decreases by 100-fold (although direct comparison is not trivial), pump power threshold increases by 10-fold, and risetimes shorten 10-fold.

Some additional understanding of the system may be gained through the analysis of the luminescence decay kinetics of $^3H_4$ level of Tm^{3+} at ca. 800 nm in PA mode (i.e. under 1059 nm excitation, **Figure S11-S12**), which are, in the first approximation, proportional to the inverse of their size. Luminescence decay kinetics were found to be dependent on pump power (**Figure S9-S10**), as previously discussed by Teitelboim *et al*.[27] This power dependence can be rationalized by the fact that PA requires efficient energy looping in the system. The energy stored in long-lived multiplets of Tm^{3+} may further modify the balance between numerous processes (i.e. luminescence decay, EM and CR) and thus may progressively recharge the emitting levels. In consequence, luminescence decay kinetics may appear longer as soon as the amount of the stored energy rises, which takes place under stronger pumping. The enhanced CR is clearly observed, because the 8% Tm^{3+} doped samples exhibit much shorter luminescence lifetimes than the 3% Tm^{3+} doped samples. Luminescence lifetimes were also found longer in cANP>csANP>μAP series of 8% Tm^{3+} samples. Moreover, it seems the EM should be *in-situ* partially diminished under strong pumping. Indeed, the luminescence lifetimes of the $^3H_4$ level get longer (e.g. 700 vs 300 μs of the short decay component and 5 vs 3.5 ms for the long decay component in 3% bulk crystal) for stronger pump powers in all samples (**Figure S6**).

2.2. Prediction of PA behavior based on modelling

Aiming to understand the role and contributions of various energy transfer processes within the energy level scheme of Tm^{3+} ions, DRE modelling was performed as described in methods section. Initially, we fixed the rates of the A_2 , A_3 , f_{ESA}, k_2 , k_3 and f_{CR} processes (shown in **Figure 4a** and explained in SI in **DRE Simulations** chapter) to values that were derived for experimentally measured pump power dependent PA emission intensity for core-shell $NaYF_4$ ANPs[21]. Briefly, A_i and k_i indicate radiative and non-radiative rates from i^{th} level. The f_{ESA} and f_{CR} factors enable to modulate the ESA and CR energy transfer rates in response to possible experimental conditions, i.e. spectral overlap of excitation laser with ESA spectrum and the variability of 'local concentration' (e.g. due to surface quenching). Next, we repeated these simulations by individually varying the respective rates. For example, radiative rate of emitting level was increased above and decreased below the original value ($A_2 = 162\ s^{-1}$), while keeping the values of all the other parameters fixed. The outcome of such simulations is

presented in **Figure 4** (A_2). This dataset enables to qualitatively understand how the changes in radiative rate of the $^3F_4$ level – i.e. A_2 affect the behavior of PA emission. It may be found that higher A_2 rates progressively enhance the slope but increase the PA threshold. Similar considerations were carried out for the other parameters of the DRE – i.e., all values except one were fixed to the pristine literature values (**Figure 4**, middle row). Because these are phenomenological parameters, one may try to optimize and enhance the features of PA emission by selection of other host materials (e.g., $NaYF_4$ vs $LiYF_4$), crystallographic structure or dopant concentration.

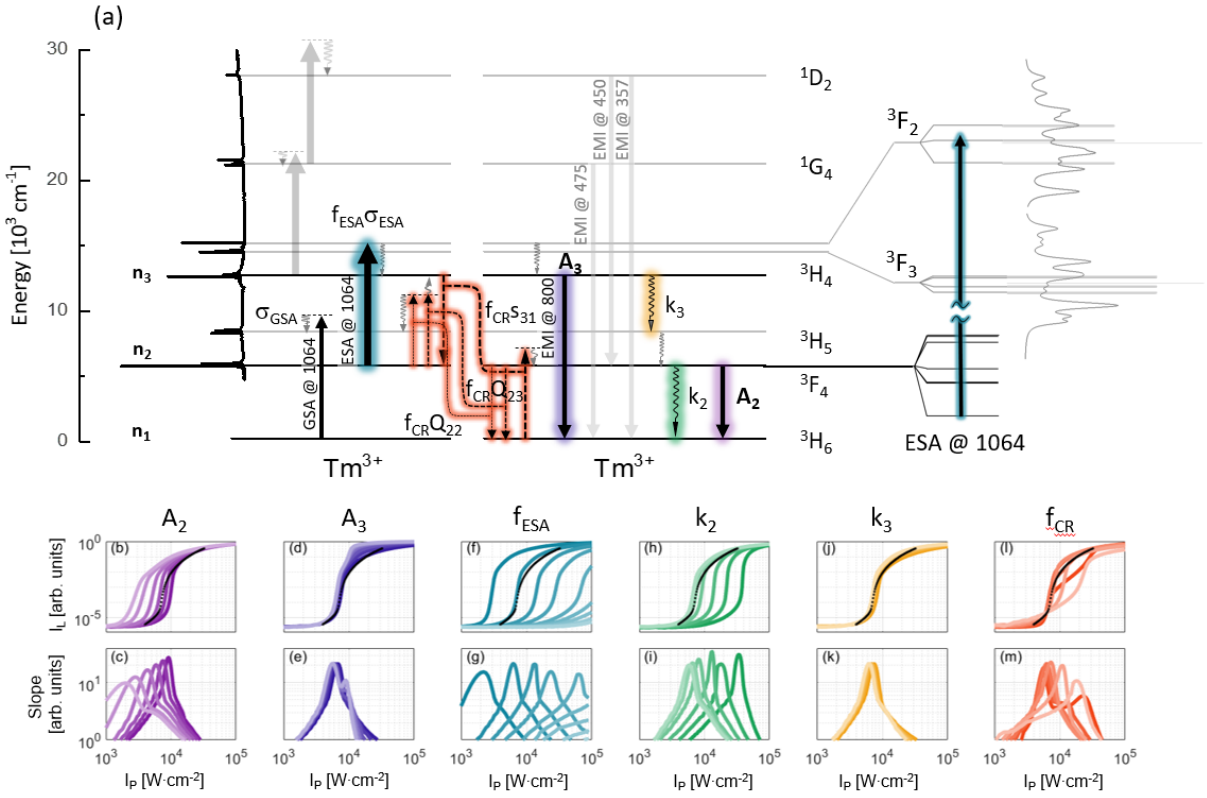

Figure 4. (top) Energy levels of Tm^{3+} with transitions leading to PA emission (a), measured ground state absorption (left) and calculated excited state absorption spectra of Tm^{3+} in $LiYF_4$ (right). **(bottom)** Simulations of PA emission behavior – PA emission intensity (middle row: b, d, f, h, j, l) and derived PA slopes (bottom row: c, e, g, i, k, m) power dependence in response to variations of phenomenological parameters: A_2 =250, 200, 150, 100, 50, 20 s^{-1}, A_3 = 1000, 500, 250, 100, 50, 25 s^{-1}, f_{ESA} = 5, 2, 1, 0.5, 0.2, 0.1, 0.05, 0.02, 0.01; k_2 = 1000, 500, 250, 100, 50, 25 s^{-1}, k_3 = 2000, 1000, 500, 250, 50, 25 s^{-1} and f_{CR} = 0.5, 0.2, 0.1, 0.05, 0.02, 0.01. The variability was applied individually to only one of the parameters at a time. Higher values correspond to more saturated color, while black dotted lines (middle row) indicate experimental data obtained in 8%Tm^{3+}-doped $NaYF_4$@$NaYF_4$ colloidal nanoparticles at RT. [21]

Numerical calculations made with DREs help to understand how the processes that contribute to the PA affect the pump-power-dependent emission intensity (**Figure 4**). Importantly, the: A_2 , A_3 , f_{ESA}, k_2 , k_3 and f_{CR} parameters can be directly related to the phenomenological features of PA materials. For example, inverses of A_2 and A_3 are spontaneous radiative lifetimes of $^3F_4$ and $^3H_4$ levels, and those can be tuned with the crystal field of the host matrix. Moreover, stronger crystal fields will generally enhance the splitting and may modify energy mismatches, which in consequence will affect the PA behavior in various temperatures [27,31]. It is well known that Tm^{3+} UV emission is more intense in $LiYF_4$ and its crystal field renders more split Stark levels of the SLJ terms.[32] This in turn will possibly make the $LiYF_4$ PA crystals more tolerant to spectral detuning of ESA from fixed wavelength lasers, but will make PA suffer from lower $\frac{\sigma_{ESA}}{\sigma_{GSA}}$. The inverses of ($A_2 + k_2$) and ($A_3 + k_3$) for these levels depend on the non-radiative multiphonon relaxation losses, which obviously will be reduced at lower temperature and for low phonon host materials. The high energy phonons will inversely enhance multi-phonon relaxation, energy transfer rates (EM, CR) and other phonon assisted energy transfers. The crystal field will most probably modify the branching ratio β_{31} of the A_3 emission, which will change the balance between the interdependent processes and will modify the energy looping and thus will affect the PA threshold. The variability of k_2 , k_3 shall also be related with enhanced loses and the surface to volume ratio, the factors that are not directly included in the DRE model. The reduced sizes of ANP and exposure of superficial PA ions to surface quenching and acceptors may also have a tremendous impact on the PA performance through the k_2 parameter as well as through the concentration dependent balance between CR and EM, to ultimately result in development of sensitive avalanche labels for biosensing of environment. [4]

Furthermore, variations in PA performance may originate from the variability of the pump power threshold, which is most strongly modified by f_{ESA}, which in turn is the result of the spectral overlap between the pumping laser and the ESA spectrum. In other words, detuning from maximum ESA will increase the threshold and will smooth the "S" shape, diminish PA features or ultimately quench the luminescence completely. This also suggests that because the same activator ions in various host matrixes may experience different Stark splitting and different crystallographic environment, new PA materials may critically require fine tuning of excitation wavelength. In some other cases, like for low A_2, low A_3 or large f_{CR}, double slope

maxima can be found at different pump power. We anticipate this is due to the relatively complex interdependence between all the phenomenological parameters. While A_2 should in principle be constant (i.e., determined by the product of $U_{2,4,6}$ *f-f* matrix elements for given transitions and phenomenological $W_{2,4,6}$ parameters for a given host) for a given activator ion in given host material, the k_2 rates may be influenced easily by surface quenchers (crystallographic defects, ligand and solvent phonons) or temperature dependent multiphonon relaxation. The population of the $^3F_4$ level may be additionally and presumably affected by other factors, such as presence of energy acceptors, physical strains in the matrix or illumination with additional MIR photons. Finally, the cross-relaxation rates, which are related to the distance between luminescent centers, and thus, phenomenologically, to the concentration of dopants, indicates sufficiently high doping is required to observe the "S" shape power dependence. While the s_{31} shall be considered constant for given concentration of dopants, the f_{CR} number has been introduced into the simulations to mimic perturbation to the energy looping like local cumulation/dilution of dopant ions or exposure to surface defect. It thus seems, the PA is quite tolerant for CR *as long as* it is efficient and doubles the population intermediate level. This is demonstrated by both the simulations and experimental results.[21] In particular, little avalanching is observed when either too little or too many Tm^{3+} ions are involved and a clear optimum can be found.

The increasing surface to volume ratio, which was investigated here using a series of materials in wide dimensionality range (from bulk through micro to nano), will be reflected in increasing the k_2 , k_3 and reducing f_{CR}. One may understand that exposing a large number of lanthanide ions (which is a prerequisite for the energy looping and PA) to the surface defects[29], clustering effects[33,34], internal residuals of OH- groups[35], surface bound ligands, and other surface perturbations, such as crystal structure modification at grain boundary[29], solvent physicochemical properties (refractive index, solvent molecules etc.)[36–38] will affect the superficial ions behavior. Nanoparticle surface passivation has proven to be an effective way to minimize surface effects, but this strategy is based on Yb^{3+}-sensitized upconversion or Gd^{3+} energy-migration mediated UC[39] and may not be directly transferrable to PA materials. This is because Yb^{3+} and Gd^{3+} ions exhibit relatively high absorption cross sections, long luminescence lifetimes, large > 9000 cm^{-1} energy gap and simple energy level scheme, which, for typical concentrations of above 20% support effective energy diffusion over even hundreds of nanometers (~140 nm was reported for Gd^{3+} network[39]). In conventional upconverting materials ET between Yb^{3+} or Gd^{3+} ions networks is responsible for energy migration. Inversely,

in photon avalanching materials, CR (between neighbor e.g., Tm^{3+} ions) rapidly depopulates the highly excited states to double the population of the intermediate excited levels. Because of weak GSA at the excitation wavelength, the PA materials are initially transparent at these wavelengths at low pumping powers. These effects further support the fact that ET plays a different and beneficial role in PA as opposed to detrimental role in conventional UC materials.

2.3. Photon Avalanche Single beam Super-resolution Imaging

To demonstrate the suitability of investigated materials for photon avalanche single beam super-resolution imaging (PASSI), we employed 3% Tm^{3+}-doped $LiYF_4$ csANP and the 1059 nm diffraction limited beam for raster scanned confocal luminescence imaging. During the measurement the power density of the laser beam used for excitation was reduced between consecutive scans (**Figure 5a-c**), starting from high powers corresponding to the PA saturation region (where, due to low S value, the PASSI concept cannot be demonstrated) down to the powers, at which the pure (i.e. without saturation) avalanching regime is observed, where the highest possible S is observed. The pump power I_P must be well optimized for effortless sub-diffraction limited imaging. Namely, while reasonable photon counts and signal-to-noise ratio require larger I_P, the augmented optical resolution is achieved only for low/medium I_P below saturation regime of the PA dependence.

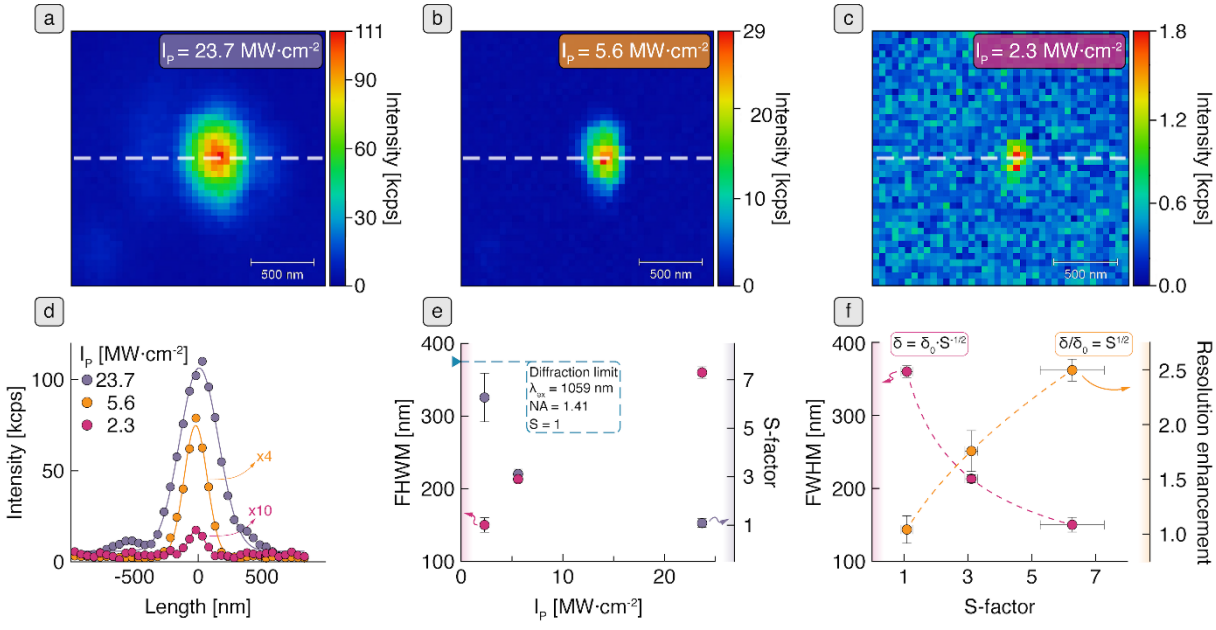

Figure 5. Demonstration of PASSI imaging on single csANP at various pumping powers. (a-c) PASSI maps for decreasing pumping intensity, (d) PA emission cross sections; emission intensities for lower excitation power densities are scaled as indicated, (e) FWHM ± standard variation (left axis) and S ± standard variation (right axis) values corresponding to these cross-

sections of the csANP and (f) comparison of changes of the imaged spot FWHM with varying S parameter (left axis) as well as the resulting resolution enhancement (right axis), respective fits are also shown.

Out of all of the nano-sized ANPs, 3% Tm^{3+} doped csANPs exhibited the most promising features for applications such as sub-diffraction PASSI.[21,22] Although they display slopes and pump thresholds similar to other 8% and 3% Tm^{3+} ANPs, they are ca. 10-100 brighter, and thin passive shells do not affect the PA threshold significantly. This insensitivity could potentially enable reduction in the size of such luminescent labels without affecting PA behavior. The medium values of $\tau_{50\%}$ ~30 ms should in principle be considered too long for raster scanned imaging, but as the diffraction limited beam scans over the sample with shorter dwell time, pre-pumping occurs to the spot next to the one being measured by the ca. 500 nm wide Gaussian beam. Indeed, the 3% Tm^{3+} csANPs have proven to enable PASSI of individual ANPs below the diffraction limit. This demonstrates that almost any confocal raster scanning microscope can be easily transformed to super-resolution one with ANPs labels.

As presented in the confocal images of a single bright spot and on the corresponding intensity profiles taken across the dotted lines (**Figure 5a-c**, red dotted line), the size of the image decreases for reduced excitation power density (**Figure 5d-f**). The full width at half maximum (FWHM) parameter starts decreasing from the expected values of a diffraction limited spot ($\delta_0 \cong 375$ nm) for higher powers (**Figure 5d**), and as soon as the excitation power density approaches the PA regime the resolution improves and the single 30 nm diameter ANP is visualized with FWHM = 150 nm. The images presented in **Figure 5** confirm the concept of PASSI [21,22] and that it is suitable to perform super-resolution imaging with Tm^{3+}-doped $LiYF_4$ host, despite the maximal obtained PA nonlinearities were only S=8-12. Although ultra-high nonlinearities (S>30 was reported for $NaYF_4$ host [21]) are obviously beneficial for the optical resolution in sub-diffraction imaging, our work further confirms the enhancement is actually quite tolerant to the nonlinearity[22] , and medium S values (S=8-12 presented here) or smaller S values (e.g. S=6.2 presented by Denkova *et al.*[23,40]) are also suitable to bring substantial imaging resolution improvements. In **Figure 5e** (right scale) are presented the values of the $S^{-1/2}$ factor (that scales Abbe diffraction limit ($\delta = \frac{\lambda}{2 \cdot NA \cdot \sqrt{S}} = \frac{\delta_0}{\sqrt{S}}$) (**Equation 6**) [22]) required to obtain observed imaging resolution improvements. They are increasing from the value of around 1 for the saturating pump power to ~6 for the image with the best resolution and still reasonable signal-to-noise ratio. It suggests that there is still room for improvement, as the

optical resolution is even more effectively enhanced for S>10 (where over 3-fold FWHM improvement is expected), while further improvements require much higher nonlinearities (over 7-fold improvement is expected from S>50). The 2.5-fold improvement in optical resolution is accompanied with ca. 6-fold luminescence intensity drop, which owes to 10-fold pump intensity decrease. The latter condition emerges from the PASSI requirement to work below saturation region[22]. Simultaneously, the signal-to-noise decreases from ca. 22 down to ca. 3.6, respectively. This is meaningful as the optical resolution, signal strength, and signal-to-noise are interconnected [22], which can be also related to the local nonlinearity slope of the power dependence relationship.

Moreover, it should be also noted that relatively high power density required to operate in the PASSI regime with the highest nonlinearity of the optical response (just above the PA threshold, in the range of MW cm^{-2} in the presented system) should not limit the use of PA for biological imaging in-vivo. First of all, the applied excitation wavelength (~1060 nm) corresponds to the transmission window of biological tissues and is poorly absorbed or scattered in cells and tissues. Moreover, these high values of power density are caused by strong (diffraction limited) focusing of the laser beam and are confined in the beam focus of ca. 350 nm diameter (~2.3 10^{-14} cm^3). Similarly, high (MW/cm^2) excitation powers are commonly used in confocal microscopy and even higher pump densities are required for 2/3-photon microscopy [41]. Moreover, bioimaging based on avalanche-like effect was already reported [23,40], and the excitation beam densities of ca. 0.1 MW/cm^2 were successfully applied in biological samples. We suppose, that the pump power threshold (ca. I_{TH} ~1 MW/cm^2) and the non-linearities (S=6-12) found here for $LiYF_4$, being different from those found in $NaYF_4$ [42] (ca. I_{TH}~10 kW/cm^2 and S=15-31) result from the fact PA efficiency is strongly susceptible to β factor (Eq.1), which apparently is more favorable in Tm^{3+}-doped $NaYF_4$ under 1064 nm excitation, than the Tm^3-doped $LiYF_4$Excited with 1059 nm. This indicates the importance of ESA absorption spectra knowledge (Figure S8) to optimize the performance of PA emission in new materials, which defines one of the most important challenges to further reduce the PA threshold below kW/cm^2 level.

3. Conclusions

In summary, understanding the relationship between the PA emission and the volume of materials has important implications for some applications in nano-bio-photonics. For that

reason, the nanomaterials (core and core-passive shell), micromaterials and bulk $LiYF_4$ crystal, all doped with 3% Tm^{3+} are compared in this work. Corresponding core-only and core-shell nanomaterials as well as microcrystals doped with 8% Tm^{3+} were also synthesized and their pump power dependent photon avalanche slopes, thresholds, gains, luminescence risetimes and decay times were quantitatively compared. The luminescence of all studied materials at 800 nm and 475 nm demonstrated all the hallmarks of photon avalanche emission – i.e., distinct pump power threshold, high 6-12 nonlinearity of PA emission, pump power dependent risetime slowdown. Beside spectroscopic characterization, photon avalanche single beam super-resolution imaging (PASSI) using 3% Tm^{3+} doped $LiYF_4$ csANPs was demonstrated, and spatial FWHM achieved was equal to 125 nm. While PASSI imaging has been previously demonstrated, the present studies highlight that even modest nonlinearities achieved in other matrices are suitable for these kinds of applications. Additionally, the photon-budget of PASSI imaging is discussed and it was found that 2.5-fold improvement in optical resolution is accompanied with ca. 6-fold luminescence intensity drop, which owes to purposeful 10-fold pump intensity decrease. To further understand the role of crystal size, differential rate-equation (DRE) PA model was evaluated based on data found for $NaYF_4$, and by modulating only one of the model parameters at a time (radiative and non-radiative rates, cross relaxations and ESA), it was possible to find that the PA emission is relatively tolerant to the variations in concentration of activator ions and radiative/non-radiative properties of the emitting level, while the perturbations applied to the population of the intermediate $^3F_4$ level (exemplified by quenching and efficient ESA excitation) are critical to achieve efficient PA emission. These findings and predictions form more solid background for development of new and further optimized PA materials and future applications of PA for mid-infrared photon counters, biosensing, optical computing, and super-resolution imaging.

4. Experimental Section

Size series of $LiYF_4$ bulk crystal, microcrystals, core nanocrystals and core-shell nanocrystals doped with either 3% or 8% Tm^{3+} were prepared to investigate the host size and architecture influence on the PA features. Bulk crystal doped with 3% of Tm^{3+} ions was reported earlier.[43] Methods of synthesis of nanocrystals and microcrystals are described in the SI. $LiYF_4$ exhibits natural birefringence, but we have purposefully used unpolarized laser excitation with a diffraction-limited beam spot (ca. 0.5 μm, see details in SI) to avoid problems with comparison between ensembles of nano- versus micro- and bulk crystals. Here tetragonal $LiYF_4$ materials

characterized by space group $I4_1/a$ (C_{4h}^6) with cell parameters a=5.164(1) Å, c=10.741(2) Å were used.[44] The studies were performed for 3% Tm^{3+}-doped bulk avalanche crystal (bAC), avalanche microcrystals (μAP), avalanche bare core nanocrystals (cANP) and core-shell nanocrystals (csANP) (**Figure 2b**). Additionally, we have investigated μAP, cANP, and csANP doped with 8% of Tm^{3+} (**Figure 2a**). All samples (summarized in Table 1) were studied with the same set of measurements made on the same optical setup, and can be directly and qualitatively compared. Firstly, pump power dependent luminescence intensity, $I_L(I_P)$, at 800 and 475 nm were collected with a home-built setup (**Figure S13**). Occasionally, these measurements were paused to collect the kinetic behavior, risetimes and decay times, of luminescence at a given pump power **(Figures S9** and **S10, Table S2**). Based on this set of experimental data, further PA parameters were derived with custom algorithms discussed in the SI. The essential one from the point of view of the PA performance was the pump power dependent slope, $S(I_P)$, resulting from the power law ($I_L(I_P) = I_P^S$) connecting the pumping power density, I_P, and luminescence intensity, $I_L(I_P)$. We have extended this analysis to consider the pump power dependent PA gain, $D_{AV}(I_P)$, as the relative PA intensity growth when doubling the pump intensity, i.e. $D_{AV}(I_P) = \frac{I_L(2I_P)}{I_L(I_P)}$ (**Equation 2**). Moreover, the dynamics of the luminescence for all the investigated structures was also measured. The risetime $t_{50\%}$ parameter was defined as the time required for PA luminescence risetime to reach 50% of steady-state luminescence intensity at a given pump intensity ($I_L(t_{50\%}) = ½\ I_L$). To better understand the observed relationships of PA emission in crystals of various size / volume, we have performed simulations of PA with differential rate equations (DRE)(SI) based on a model originally develop for NaYF4 nanoparticles.[21] PASSI imaging was performed on a customized optical confocal microscope using single excitation beam at 1059 and monitoring 800 nm emission of Tm^{3+} ions (SI).

Acknowledgements

The authors acknowledge financial support from projects 2018/31/B/ST5/01827, 2017/26/E/ST3/00209, and 2018/31/G/ST3/03596 funded by the National Science Center. Work at the Molecular Foundry was supported by the Office of Science, Office of Basic Energy Sciences, of the U.S. Department of Energy under Contract No. DE-AC02-05CH11231. Calculations have been carried out using resources provided by Wroclaw Centre for Networking and Supercomputing (http://wcss.pl), grant No. 529. A. S. acknowledges the support from the European Union's Horizon 2020 research and innovation program under the

Marie Skłodowska-Curie grant agreement No. 895809 (MONOCLE). PJS acknowledge support from the Global Research Laboratory (GRL) Program through the National Research Foundation of Korea (NRF) that is funded by the Ministry of Science and ICT (2016911815), KRICT (KK2061-23, SKO1930-20).

References

[1] J. C. G. Bünzli, S. Comby, A. S. Chauvin, C. D. B. Vandevyver, *Journal of Rare Earths* **2007**, *25*, 257.
[2] F. Auzel, *Chemical Reviews* **2004**, *104*, 139.
[3] M.-F. F. Joubert, *Opt Mater (Amst)* **1999**, *11*, 181.
[4] A. Bednarkiewicz, E. M. Chan, K. Prorok, *Nanoscale Advances* **2020**, *2*, DOI 10.1039/d0na00404a.
[5] K. W. C. Kwock, C. Lee, A. Teitelboim, Y. Liu, K. Yao, S. B. Alam, B. E. Cohen, E. M. Chan, P. J. Schuck, *Journal of Physical Chemistry C* **2021**, *125*, DOI 10.1021/acs.jpcc.1c07721.
[6] M. Szalkowski, M. Dudek, Z. Korczak, C. Lee, Ł. Marciniak, E. M. Chan, P. J. Schuck, A. Bednarkiewicz, *Optical Materials: X* **2021**, *12*, 100102.
[7] J. S. Chivian, W. E. Case, D. D. Eden, *Applied Physics Letters* **1979**, *35*, 124.
[8] W. Lenth, R. M. M. Macfarlane, *Journal of Luminescence* **1990**, *45*, 346.
[9] H. Wen, H. Zhu, X. Chen, T. F. Hung, B. Wang, G. Zhu, S. F. Yu, F. Wang, *Angewandte Chemie - International Edition* **2013**, *52*, 13419.
[10] F. Wang, R. Deng, J. Wang, Q. Wang, Y. Han, H. Zhu, X. Chen, X. Liu, *Nature Materials* **2011**, *10*, 968.
[11] X. Xie, N. Gao, R. Deng, Q. Sun, Q. H. Xu, X. Liu, *J Am Chem Soc* **2013**, *135*, 12608.
[12] C. Zhang, J. Y. Lee, *ACS Nano* **2013**, *7*, 4393.
[13] S. Fischer, N. D. Bronstein, J. K. Swabeck, E. M. Chan, A. P. Alivisatos, *Nano Letters* **2016**, *16*, 7241.
[14] A. Pilch, C. Würth, M. Kaiser, D. Wawrzyńczyk, M. Kurnatowska, S. Arabasz, K. Prorok, M. Samoć, W. Strek, U. Resch-Genger, A. Bednarkiewicz, *Small* **2017**, *13*, 1770246.
[15] Q. Su, S. Han, X. Xie, H. Zhu, H. Chen, C. K. Chen, R. S. Liu, X. Chen, F. Wang, X. Liu, *J Am Chem Soc* **2012**, *134*, 20849.
[16] G. Ledoux, D. Amans, M.-F. Joubert, B. Mahler, S. Mishra, S. Daniele, C. Dujardin, *Journal of Physical Chemistry C* **2017**, *122*, 888.
[17] L. Tu, X. Liu, F. Wu, H. Zhang, *Chemical Society Reviews* **2015**, *44*, 1331.
[18] F. Wang, R. Deng, J. Wang, Q. Wang, Y. Han, H. Zhu, X. Chen, X. Liu, *Nature Materials* **2011**, *10*, 968.
[19] T. Wang, H. Zhou, Z. Yu, G. Zhou, J. Zhou, D. Huang, L. Sun, P. Gao, Y. Sun, J. Hu, *The Journal of Physical Chemistry C* **2018**, *122*, 10113.
[20] A. Pilch-Wrobel, A. Kotulska, S. Lahtinen, T. Soukka, A. Bednarkiewicz, *Small* **2022**.
[21] C. Lee, E. Z. Xu, Y. Liu, A. Teitelboim, K. Yao, A. Fernandez-Bravo, A. M. Kotulska, S. H. Nam, Y. D. Suh, A. Bednarkiewicz, B. E. Cohen, E. M. Chan, P. J. Schuck, *Nature* **2021**, *589*, 230.
[22] A. Bednarkiewicz, E. M. Chan, A. Kotulska, L. Marciniak, K. Prorok, *Nanoscale Horizons* **2019**, *4*, 881.

[23] D. Denkova, M. Ploschner, M. Das, L. M. Parker, X. Zheng, Y. Lu, A. Orth, N. H. Packer, J. A. Piper, *Nature Communications* **2019**, *10*, 1.
[24] L. Marciniak, A. Bednarkiewicz, K. Elzbieciak, *Journal of Materials Chemistry C* **2018**, *6*, 7568.
[25] M. You, J. Zhong, Y. Hong, Z. Duan, M. Lin, F. Xu, *Nanoscale* **2015**, *7*, 4423.
[26] A. Fernandez-Bravo, K. Yao, E. S. Barnard, N. J. Borys, E. S. Levy, B. Tian, C. A. Tajon, L. Moretti, M. Virginia Altoe, S. Aloni, K. Beketayev, F. Scotognella, B. E. Cohen, E. M. Chan, P. James Schuck, **n.d.**, DOI 10.1038/s41565-018-0161-8.
[27] A. Teitelboim, B. Tian, D. J. Garfield, A. Fernandez-Bravo, A. C. Gotlin, P. J. Schuck, B. E. Cohen, E. M. Chan, *Journal of Physical Chemistry C* **2019**, *123*, 2678.
[28] J. Fan, L. Liang, Y. Gu, X. Liu, *Optical Materials: X* **2021**, *12*, 100104.
[29] H. Xu, S. Han, R. Deng, Q. Su, Y. Wei, Y. Tang, X. Qin, X. Liu, *Nature Photonics 2021 15:10* **2021**, *15*, 732.
[30] D. Hudry, A. de Backer, R. Popescu, D. Busko, I. A. Howard, S. Bals, Y. Zhang, A. Pedrazo-Tardajos, S. van Aert, D. Gerthsen, T. Altantzis, B. S. Richards, *Small* **2021**, *17*, 2104441.
[31] E. S. Levy, C. A. Tajon, T. S. Bischof, J. Iafrati, A. Fernandez-Bravo, D. J. Garfield, M. Chamanzar, M. M. Maharbiz, V. S. Sohal, P. J. Schuck, B. E. Cohen, E. M. Chan, *ACS Nano* **2016**, *10*, 8423.
[32] B. Venkataramanan Mahalingam, F. Vetrone, R. Naccache, A. Speghini, J. A. Capobianco, J. A. Capobianco, V. Mahalingam, F. Vetrone, R. Naccache, A. Speghini DiSTeMeV, U. di Verona, U. Verona Verona, *Adv. Mater* **2009**, *21*, 4025.
[33] J. Wang, R. Deng, M. A. Macdonald, B. Chen, J. Yuan, F. Wang, D. Chi, T. S. Andy Hor, P. Zhang, G. Liu, Y. Han, X. Liu, *Nature Materials* **2014**, *13*, 157.
[34] F. Auzel, P. Goldner, *Opt Mater (Amst)* **2001**, *16*, 93.
[35] Y. Feng, Z. Li, Q. Li, J. Yuan, L. Tu, L. Ning, H. Zhang, *Light: Science & Applications 2021 10:1* **2021**, *10*, 1.
[36] M. Kraft, C. Würth, V. Muhr, T. Hirsch, U. Resch-Genger, *Nano Research* **2018**, *11*, 6360.
[37] F. T. Rabouw, P. T. Prins, P. Villanueva-Delgado, M. Castelijns, R. G. Geitenbeek, A. Meijerink, *ACS Nano* **2018**, *12*, 4812.
[38] C. Würth, S. Fischer, B. Grauel, A. P. Alivisatos, U. Resch-Genger, *J Am Chem Soc* **2018**, *140*, 4922.
[39] R. Deng, J. Wang, R. Chen, W. Huang, X. Liu, *J Am Chem Soc* **2016**, *138*, 15972.
[40] M. Plöschner, D. Denkova, S. de Camillis, M. Das, L. M. Parker, X. Zheng, Y. Lu, S. Ojosnegros, J. A. Piper, *Optics Express* **2020**, *28*, 24308.
[41] L. Schermelleh, R. Heintzmann, H. Leonhardt, *Journal of Cell Biology* **2010**, *190*, 165.
[42] C. Lee, E. Z. Xu, Y. Liu, A. Teitelboim, K. Yao, A. Fernandez-Bravo, A. M. Kotulska, S. H. Nam, Y. D. Suh, A. Bednarkiewicz, B. E. Cohen, E. M. Chan, P. J. Schuck, *Nature* **2021**, *589*, 230.
[43] V. François, F. Pellé, P. Goldner, D. Simkin, *Journal of Luminescence* **1995**, *65*, 57.
[44] A. Grzechnik, K. Syassen, I. Loa, M. Hanfland, J. Y. Gesland, *Physical Review B* **2002**, *65*, 104102.